

Uncertainty Quantification for Hyperspectral Image Denoising Frameworks based on Low-rank Matrix Approximation

Shaobo Xia*, Jingwei Song*, Dong Chen, Jun Wang

Abstract—Low-rank matrix approximation (LRMA) is a technique widely applied in hyperspectral images (HSI) denoising or completion. The uncertainty quantification of the estimated restored HSI, however, has not been addressed in previous researches. The lack of uncertainty of the product significantly limits the applications like multi-source or multi-scale data fusion, data assimilation and product confidence quantification, since these applications require an accurate way to describe the statistical distributions of the source data. To address this issue, we propose a prior-free closed-form element-wise uncertainty quantification method for the LRMA based HSI restoration. The proposed approach only requires the uncertainty of the observed HSI and can yield uncertainty in a limited amount of time and with similar time complexity comparing to the LRMA technique. We conduct extensive experiments to validate that the closed-form uncertainty describes the estimation accurately, is robust to at least 10% ratio of random impulse noises and takes only around 10–20% amount of time of LRMA. All the experiments indicate that the proposed closed-form uncertainty quantification method is more applicable to be deployed to real-world applications than the baseline Monte-Carlo tests.

Index Terms—Low-rank matrix approximation, hyperspectral images, uncertainty quantification.

I. INTRODUCTION

Data uncertainty, which refers to the lack of sureness about the data [1], is an essential factor to be considered when utilizing remote sensing data and their derived products [2]. Given data uncertainties, users can determine whether a product is applicable in their applications, or how to balance the contributions of different data. For example, the minimum detectable deformation can be estimated based on uncertainty measures in point clouds, based on which engineers can make a proper project plane, including sensor selection and set-up schemes [3]. In multiple data fusion tasks, the label uncertainties of HSI and point clouds are often considered to achieve high fusion accuracy [4].

Uncertainty can be classified as aleatoric uncertainty and epistemic uncertainty. The aleatoric uncertainty is caused by

the noise existed in both data collections and processing steps while the epistemic uncertainty is caused by the observation models and data post-processing methods [1]–[3], [5], [6]. In the scenario of absent of ground truth to measure the performance of the model, the epistemic uncertainty is normally ignored and the output uncertainty is defined as the aleatoric uncertainty with the propagation of the arbitrary model. Most researches define the probabilistic density function of the noise as a mixture of normal distribution and random distribution. By ignoring the random noise, the uncertainty is to describe the normal distribution. In HSI restoration, symmetric uncertainty based on mutual information is proposed in [7], and applied to hyperspectral images (HSI) classifications. In HSI unmixing, the end member uncertainty for those unmixing methods based on the normal compositional model is defined as a covariance matrix, based on which unmixing errors can be predicted without knowing the ground truth [8]. In other researches, the description of the uncertainty is presented in different forms. In [1], an entropy-based uncertainty measure is proposed for the evaluation of the classification results of multi-spectral remote sensing images. The calculated entropy is based on all the classification results would be high if the pixel-wise classification uncertainty is high. In [9], the uncertainty of 3D point clouds is defined as the measurement repeatability, realized by the median and two percentiles (5% and 95%) related to repeated measurements.

This paper focuses on the uncertainty quantification in the HSI denoising domain. HSI that consists of hundreds or thousands of spectral bands, has been widely used in various applications (e.g., land cover mapping), attributing to its rich spectral information beyond the spatial information. In HSI data processing, image denoising as an important preprocessing step for advanced applications is attracting lots of concerns in past decades [10]. According to [11], the exiting HSI denoising methods can be categorized into three groups, filter-based methods, model optimization-based methods, and deep learning-based methods. Filter-based methods try to remove noise based on various filters. Classical methods in this category are based on nonlocal filters [12]–[15]. The model optimization-based methods can be further divided into several classes such as total-variation methods [16], sparse representation-based [17], and low-rank matrix-based methods [18]. The major advantages of this group of denoising methods are utilizing image priors and considering spatial and spectral features simultaneously. These methods are often combined to achieve better performance [19], [20]. The last group

* the authors contribute equally to this paper.

Jingwei Song is with the Centre for Autonomous Systems, University of Technology, Sydney, P.O. Box 123, Broadway, NSW 2007, Australia. e-mail: (jingwei.song@student.uts.edu.au).

Dong Chen is with the College of Civil Engineering, Nanjing Forestry University, Nanjing 210037, China. e-mail: (chendong@njfu.edu.cn).

Jun Wang is with the Institute of Remote Sensing and Digital Earth, Chinese Academy of Sciences, University of Chinese Academy of Sciences, Beijing, China. e-mail: (wangjun@radi.ac.cn).

Shaobo Xia is with the Department of Geomatics Engineering, University of Calgary, T2N 1N4, Canada. e-mail: (shaobo.xia@ucalgary.ca).

of methods is based on deep learning frameworks and is attracting rising attention in the past three years [21]. In this group, a recent deep learning-based framework is proposed in [11], which can remove hybrid noise under a spatial-spectral framework.

In recent years, lots of HSI denoising studies are based on the low-rank matrix approximation (LRMA) framework which has become a state-of-the-art technique in this research area [18], [22]. These methods belong to the second category (i.e., the model optimization-based methods), and the basic idea is exploiting the low-dimensional structure in the high dimensional data space. The LRMA based studies [18], [19], [23] held the prior that the noise-free HSI can be represented by the low-rank matrices. Thus, the HSI denoising can be viewed from a classical low-rank matrix recovery problem. A representative HSI denoising framework based on LRMA is described in [18], where clean image, mixed noise, and Gaussian noise were formulated separately in their objective function which was minimized under low-rank constraints. There are many variants of LRMA-based HSI denoising methods presented in the past five years [19], [22], [24]–[26]. For example, [22] proposed an LRMA-based framework that contains a term named total-variation regularization aiming at preserving spatial information. The spatial-spectral structural in HSI denoising is also exploited via replacing low-rank matrix analysis by low-rank tensor approximation [26]. In general, LRMA-based HSI denoising methods can be treated as the state-of-the-art framework which has been widely applied in this area.

Despite the progress in LRMA-based HSI denoising, no research pays attention to the uncertainty quantification of these denoised HSI. Several existing works aim at estimating the noise of the raw observation [27], [28] while the confidence of the denoised HSI has been overlooked, which is critical in further applications as pointed at the beginning of this paper. However, the quantification of uncertainties for the denoised HSI based on LRMA is difficult due to the nonlinear functions in LRMA models (e.g., nuclear norm), which makes it hard to deduce the closed-form uncertainty propagation formulations. Recently, [29] proposed an optimal uncertainty quantification and inference method for noisy matrix completion. Inspired by this work, we find that it would be possible to obtain quantified uncertainties of outputs from LRMA-based HSI denoising frameworks.

In this work, we will focus on the formulation of denoising uncertainties in terms of Gaussian noise. As described in [14], [19], [28], Poisson noise is the main concern in real HSI data and can be approximated by the additive Gaussian noise, which can be precisely described by mean and covariances, making it possible to build uncertainty propagation models.

To sum up, the main contributions of this paper are two-fold,

- 1) To the best of our knowledge, the uncertainty quantification for denoised HSI based on LRMA is presented for the first time in this paper. We provide a closed-form time-efficient uncertainty propagation model to predict element-wise uncertainty for denoised HSI without knowing any ground-truth.

- 2) The proposed uncertainty estimation approach is independent of the choice of the LRMA algorithm. It is based on the global minimum assumption of LRMA, thus more accurate algorithm leads to better performance of the uncertainty estimation.

The rest of this paper is organized as follows. In Section II, the formulation for the uncertainty propagation under a classical LRMA-based HSI denoising framework is described in detail. Section III shows several experiments on both simulated and real HSI data. The discussions on parameter settings and limitations are presented in Section III. Section IV summarizes this paper and gives several suggestions on future works.

II. METHODOLOGY

A. Revisiting the general hyperspectral restoration process.

Fig. 1 demonstrates the routine process of the LMRA based hyperspectral image restoration. The hyperspectral image is processed with a 3D sliding window to save the computational burden. For each 3D patch within the window, all the bands are vectorized and stacked into the 2D matrix. The permuted 2D matrix goes through the routine LMRA process, and the result is re-permuted to recover the 3D denoised patch. Finally, all the patches are summarized and averaged to build the restored HSI.

The HSI acquired by the sensor is normally modeled as the image composed of Gaussian noise and random noise:

$$\mathbf{W} = \mathbf{W}^* + \mathbf{G} + \mathbf{N} \quad (1)$$

where $\mathbf{W} \in \mathbb{R}^{M \times N \times P}$ is the image acquired from the hyperspectral sensor with the size $M \times N$ and P channels, $\mathbf{W}^* \in \mathbb{R}^{M \times N \times P}$ is the noise-free image denoted as the ground truth, $\mathbf{G} \in \mathbb{R}^{M \times N \times P}$ is the element-wise, independent and identically distributed Gaussian noise and $\mathbf{N} \in \mathbb{R}^{M \times N \times P}$ is the random noise (impulse signal). The random noise \mathbf{N} is normally considered as negligible with regard to \mathbf{G} , and the data quality quantification process is inferring the statistic distribution of the \mathbf{G} . In practice, the ground truth HSI \mathbf{W}^* is not able to be obtained. Thus, we denote $\hat{\mathbf{W}}$ as the estimated denoised HSI calculated from researches based on the low-rank assumption [19], [20].

The goal of HSI denoising is to recover the denoised $\hat{\mathbf{W}}$ with the 3D HSI noisy observation \mathbf{W} and the exact rank prior. Assuming the random noise \mathbf{N} is negligible, the restored image $\hat{\mathbf{W}}$ is recovered with the following formulation:

$$\min_{\hat{\mathbf{W}}} \mu \text{rank}(\hat{\mathbf{W}}^\#) + \|\mathbf{G}\|_0, \text{ s.t. } \hat{\mathbf{W}} = \mathbf{W} + \mathbf{G} \quad (2)$$

such that $\hat{\mathbf{W}}^\# = g(\hat{\mathbf{W}})$

where μ is the hyperparameter balancing the two terms. $\text{rank}(\cdot)$ constraints the rank of the input matrix to be the no greater than the given rank. $g(\cdot)$ permute the 3D HSI to 2D matrix by vectorizing and concatenate to general 2D matrix (Fig. 1). The low-rank formulation is originally proposed by [30] and named as the ‘‘robust principal component analysis (RPCA)‘‘.

HSI restoration differs greatly conventional image processing community due to the size of data. The extremely

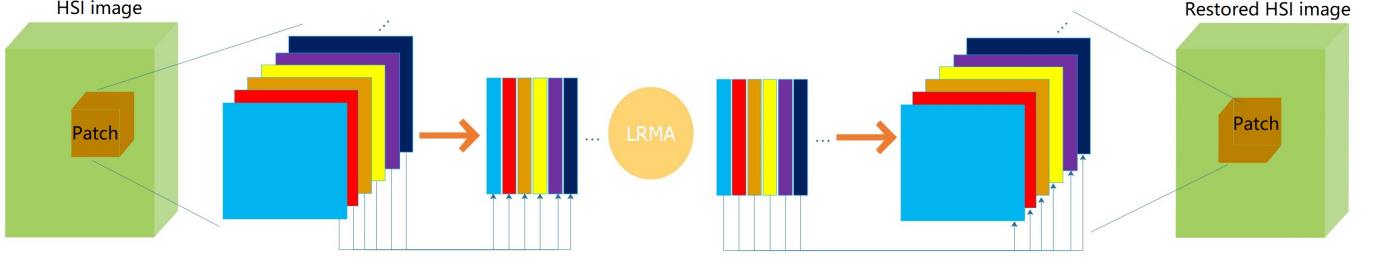


Fig. 1: Illustrated is the routine process of hyperspectral image restoration. The 3D matrix on both ends is the hyperspectral image.

large permuted 2D image hinders the regular Singular Value Decomposition (SVD) process which is essential in solving Eq. (2). To overcome the heavy computational burden in minimizing the objective function due to huge HSI size, the original HSI is segmented to small patches (denoted as the overlapped sliding window) and solved in parallel. Moreover, considering the nonconvexity of the low-rank constraint $\text{rank}(\cdot)$, the low-rank constraint is approximated with the nuclear norm constraint for efficient convex optimization. Therefore, the sliding window version of Eq. (2) is minimizing all patches:

$$\begin{aligned} \min_{\hat{\mathbf{W}}^{(ijk)}} \quad & \mu \|\hat{\mathbf{W}}^{\#(ijk)}\|_* + \frac{1}{2} \|\mathbf{W}^{(ijk)} - \hat{\mathbf{W}}^{(ijk)}\|_F^2 \\ \text{such that} \quad & \hat{\mathbf{W}}^{\#(ijk)} = g(\hat{\mathbf{W}}^{(ijk)}) \\ & (i, j, k) \in \Omega, \end{aligned} \quad (3)$$

where the matrices $\mathbf{W}^{(ijk)}$, $\hat{\mathbf{W}}^{(ijk)}$ and $\hat{\mathbf{W}}^{\#(ijk)} \in \mathbb{R}^{K \times L}$ are the patch indexed in (ijk) with regard to \mathbf{W} , $\hat{\mathbf{W}}$ and $\hat{\mathbf{W}}^{\#}$. (K, L) is the size of the permuted matrix $\hat{\mathbf{W}}^{\#(ijk)}$. $\Omega \subseteq \{1, \dots, M'\} \times \{1, \dots, N'\} \times \{1, \dots, P'\}$ is the number of patches within the size of HSI. $\|\cdot\|_F$ is the Frobenius norm minimizing the divergence of the restored HSI patch $\hat{\mathbf{W}}^{(ijk)}$ and the observation $\mathbf{W}^{(ijk)}$. After all the patches are optimized, the optimal $\hat{\mathbf{W}}$ is constructed by averaging $\hat{\mathbf{W}}^{(ijk)}$ element-wisely. By ignoring the random noise, we have the element-wise Gaussian error of the observation:

$$\mathbf{W}^{\#(ijk)} \approx \mathbf{W}^{*(ijk)} + \mathbf{G}^{(ijk)}, \quad \mathbf{G}^{(ijk)} \overset{\text{i.i.d.}}{\sim} \mathcal{N}(0, \sigma_0^2), \quad (4)$$

where σ_0^2 is the variance of the noise obtained from image or estimated by algorithms like [23]. In previous studies, the choice of rank is often estimated by manual-tuning strategies based on the differences between the reconstructed signal and the original one [19].

The idea of Eq. (3) is to convert the 3D patch into a typical 2D matrix so that the conventional LRMA algorithm can handle. It is often solved with Lagrange multiplier or Augmented Lagrange multiplier (ALM) and there is numerous off-the-shelf derivated solver. In this work, we choose the GoDec algorithm proposed by [31] to be consistent with the baseline method [18]. But we would like to address that the proposed uncertainty quantification method is independent of the solver since it only assumes the LRMA yields the global

minimum. The better solution the low-rank solver provide, the more accurate uncertainty our method describes.

After all small overlapped patches go through the process of Eq. (3), the restored denoised patches are summed up to restore the HSI:

$$\hat{\mathbf{W}} = \left[\sum_{i,j,k \in \Omega} f(\hat{\mathbf{W}}^{(ijk)}) \right] \oslash \mathbf{Q}, \quad (5)$$

where $f(\cdot)$ is the padding function to convert the patch to the same size of $\hat{\mathbf{W}}$ by padding with 0. The matrix \mathbf{Q} counts the number of elements accumulated by patches. \oslash is the Hadamard division defining the element-wise division.

B. The general framework of the closed-form uncertainty quantification algorithm

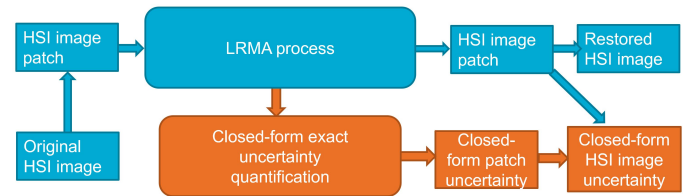


Fig. 2: The general framework of the proposed approach. Blue is the typical LRMA process ([18] as an example). Our work aims at providing an extra module to quantify the uncertainty of the output, the restored HSI, from the process of LRMA.

Fig. 2 demonstrates the general framework as well as the relationship with the routine LRMA approaches. In the LRMA process, the temporary variable, 2D low-rank matrix, is utilized to provide the uncertainty to the HSI patch-based on our closed-form formulation. After the HSI patch and its associated closed-form uncertainty are generated, the routine LRMA approach averages them to yield the restored HSI, and we correspondingly provide a closed-form uncertainty propagation to quantify the final restored HSI. As demonstrated in Fig. 2, through all the processes, the proposed approach is independent of the choice of low-rank solver. It can be easily integrated into the derivations of the LRMA process. Moreover, since our method is a closed-form solution and

only utilize the temporary variables, the processing time is small comparing to the routine LRMA process.

The major contribution our this work is that it provides an element-wise closed-form solution to quantify the uncertainty in a time-efficient manner. For the restored HSI $\hat{\mathbf{W}}$, one straight forward way of element-wise uncertainty quantification is conducting the Monte-Carlo test with the given statistical distribution of observation \mathbf{W} . However, the size of HSI is notoriously large, and it poses a heavy computational burden to conduct a massive amount of Monte-Carlo test. Rough time consumption of the processed described in [18] on $100 \times 100 \times 100$ HSI takes 20 minutes with a common commercial desktop. While a convincing uncertainty quantification requires a reasonable number of trials, the Monte-Carlo test is inefficient to be applied for element-wise HSI uncertainty quantification.

C. Uncertainty quantification for exact low-rank factorization

This section focuses on solving the uncertainty quantification for low-rank factorization process (Eq. (3)), and HSI patch-based averaging (Eq. (5)) will be discussed in next section. Recently [29] proposes an uncertainty quantification method for exact low-rank 2D matrix. This element-wise algorithm can quantify the confidence for a common low-rank based 2D matrix denoising algorithm. Synthetic and real-world tests validate the efficiency of this method. We introduce this approach and modify it to quantify the uncertainty of each estimated HSI patch $\hat{\mathbf{W}}^{(ijk)}$ from Eq. (3).

In the patch optimization process shown in Eq. (3), we first aim to quantify the uncertainty of the temporary 2D square matrix $\hat{\mathbf{W}}^{(ijk)}$ ($\hat{\mathbf{W}}^{(ijk)} = g(\hat{\mathbf{W}}^{(ijk)})$) and it can be any specific $\hat{\mathbf{W}}^{(ijk)}$. We denote the ground truth of $\hat{\mathbf{W}}^{(ijk)}$ and $\hat{\mathbf{W}}^{(ijk)}$ as $\mathbf{W}^{\#(ijk)}$ and $\mathbf{W}^{*(ijk)}$. For the sake of conciseness, the rank- r SVD decomposition is $\mathbf{W}^{\#(ijk)} = \mathbf{U}\Sigma^{\#}\mathbf{V}^{\#T}$. Two matrices are defined as the product of the unitary matrix and the squared singular matrix: $\mathbf{X}^* \triangleq \mathbf{U}^*\Sigma^{*1/2} \in \mathbb{R}^{K \times r}$, $\mathbf{Y}^* \triangleq \mathbf{V}^*\Sigma^{*1/2} \in \mathbb{R}^{L \times r}$. The following rules apply:

$$\mathbf{X}^{*T}\mathbf{X}^* = \mathbf{Y}^{*T}\mathbf{Y}^* = \Sigma^{\#*}. \quad (6)$$

Following the above definition, the ground truth 2D temporary matrix $\mathbf{W}^{\#(ijk)} = \mathbf{X}^*\mathbf{Y}^{*T}$. Similarly, we define $\hat{\mathbf{W}}^{(ijk)} \approx \hat{\mathbf{X}}\hat{\mathbf{Y}}^T$ where $\hat{\mathbf{X}}$ and $\hat{\mathbf{Y}}$ are the approximate matrices of \mathbf{X}^* and \mathbf{Y}^* . We also define:

$$\Sigma^{\#} = \hat{\mathbf{X}}^T\hat{\mathbf{X}} = \hat{\mathbf{Y}}^T\hat{\mathbf{Y}} \approx \Sigma^{\#*}. \quad (7)$$

Theorem 1. For the estimations of the auxiliary matrices $\hat{\mathbf{X}}$ and $\hat{\mathbf{Y}}$, the difference to the rectified ground truth $\hat{\mathbf{X}}$ and $\hat{\mathbf{Y}}$ are:

$$\begin{aligned} \hat{\mathbf{X}}\hat{\mathbf{R}} - \mathbf{X}^* &= \mathbf{Z}_X + \Psi_X \\ \hat{\mathbf{Y}}\hat{\mathbf{R}} - \mathbf{Y}^* &= \mathbf{Z}_Y + \Psi_Y \end{aligned} \quad (8)$$

where $\hat{\mathbf{R}}$ ($\hat{\mathbf{R}}\hat{\mathbf{R}}^T = \mathbf{I}$) is the rectification matrix to rectify $(\hat{\mathbf{X}}, \hat{\mathbf{Y}})$ to $(\mathbf{X}^*, \mathbf{Y}^*)$. The rows of the error matrix $\mathbf{Z}_X \in \mathbb{R}^{K \times r}$ (resp. $\mathbf{Z}_Y \in \mathbb{R}^{L \times r}$) are independent and obeys:

$$\begin{aligned} \mathbf{Z}_X^T \mathbf{e}_v &\stackrel{\text{i.i.d.}}{\sim} \mathcal{N}(0, \sigma_0^2(\Sigma^{\#*})^{-1}), \quad \text{for } 1 \leq j \leq K \\ \mathbf{Z}_Y^T \mathbf{e}_v &\stackrel{\text{i.i.d.}}{\sim} \mathcal{N}(0, \sigma_0^2(\Sigma^{\#*})^{-1}), \quad \text{for } 1 \leq j \leq K \end{aligned} \quad (9)$$

where \mathbf{e}_v is the basis vector and $\Psi_X, \Psi_Y \in \mathbb{R}^{K \times r}$ are the residual matrices.

The residual noises Ψ_X and Ψ_Y are significantly smaller than \mathbf{Z}_X and \mathbf{Z}_Y and Eq. (8) is approximated to:

$$\begin{aligned} \hat{\mathbf{X}}\hat{\mathbf{R}} - \mathbf{X}^* &\approx \mathbf{Z}_X \\ \hat{\mathbf{Y}}\hat{\mathbf{R}} - \mathbf{Y}^* &\approx \mathbf{Z}_Y \end{aligned} \quad (10)$$

Assuming that the first-order expansion is reasonably tight, the element-wise error between the estimation $\hat{\mathbf{W}}_{uv}^{\#(ijk)}$ and the ground truth $\mathbf{W}_{uv}^{\#(ijk)}$ at the position uv is:

$$\begin{aligned} \hat{\mathbf{W}}_{uv}^{\#(ijk)} - \mathbf{W}_{uv}^{\#(ijk)} &= [\mathbf{e}_u^T \hat{\mathbf{X}}\hat{\mathbf{R}}(\hat{\mathbf{Y}}\hat{\mathbf{R}}^T) \mathbf{e}_v - \mathbf{e}_u^T (\mathbf{X}^*\mathbf{Y}^{*T}) \mathbf{e}_v] \\ &\approx [\mathbf{e}_u^T (\hat{\mathbf{X}}\hat{\mathbf{R}} - \mathbf{X}^*)\mathbf{Y}^{*T} \mathbf{e}_v + \mathbf{e}_u^T \mathbf{X}^*(\hat{\mathbf{Y}}\hat{\mathbf{R}} - \mathbf{Y}^{*T}) \mathbf{e}_v] \\ &\approx [\mathbf{e}_u^T (\mathbf{Z}_X \mathbf{Y}^{*T}) \mathbf{e}_v + \mathbf{e}_u^T (\mathbf{X}^* \mathbf{Z}_Y^T) \mathbf{e}_v] \end{aligned} \quad (11)$$

where the bases $\mathbf{e}_u, \mathbf{e}_v$ localize the elements involved in calculating element in position (i, j) . After some manipulation, we have the element-wise variance of the error as:

$$\begin{aligned} \text{Var}(\hat{\mathbf{W}}_{uv}^{\#(ijk)} - \mathbf{W}_{uv}^{\#(ijk)}) &\stackrel{(i)}{\approx} [\text{Var}(\mathbf{e}_u^T (\mathbf{Z}_X \mathbf{Y}^{*T}) \mathbf{e}_v) + \text{Var}(\mathbf{e}_u^T (\mathbf{X}^* \mathbf{Z}_Y^T) \mathbf{e}_v)] \\ &\stackrel{(ii)}{=} \sigma_0^2 [\mathbf{e}_v^T \mathbf{Y}^* (\Sigma^{\#*})^{-1} \mathbf{Y}^{*T} \mathbf{e}_v + \\ &\quad \mathbf{e}_u^T \mathbf{X}^* (\Sigma^{\#*})^{-1} \mathbf{X}^{*T} \mathbf{e}_u] \\ &\stackrel{(iii)}{=} \sigma_0^2 (\|\mathbf{U}_{u\cdot}^*\|_2^2 + \|\mathbf{V}_{v\cdot}^*\|_2^2) \approx \sigma_0^2 v_{uv}^* \end{aligned} \quad (12)$$

where (i) is from the **theorem 1** since \mathbf{Z}_X and \mathbf{Z}_Y are nearly independent. (ii) is from the Eq. (8). (iii) $\mathbf{U}_{u\cdot}^*$ and $\mathbf{V}_{v\cdot}^*$ are the i/j th row of \mathbf{U}^* and \mathbf{V}^* . For conciseness, we define $v_{uv}^* = (\|\mathbf{U}_{u\cdot}^*\|_2^2 + \|\mathbf{V}_{v\cdot}^*\|_2^2)$. $\text{Var}(\cdot)$ is the variance of the input.

In practice, the rows of the ground truth $\mathbf{U}_{u\cdot}^*$ and $\mathbf{V}_{v\cdot}^*$ are impossible to obtain, we approximate them with the estimated version $\hat{\mathbf{U}}_{u\cdot}$ and $\hat{\mathbf{V}}_{v\cdot}$, which are the i/j th row of the estimations $\hat{\mathbf{U}}$ and $\hat{\mathbf{V}}$. Thus the element-wise variance can be approximated as:

$$\text{Var}(\hat{\mathbf{W}}_{uv}^{\#(ijk)} - \mathbf{W}_{uv}^{\#(ijk)}) \approx \sigma_0^2 (\|\hat{\mathbf{U}}_{u\cdot}\|_2^2 + \|\hat{\mathbf{V}}_{v\cdot}\|_2^2) = \sigma_0^2 \hat{v}_{uv} \quad (13)$$

where \hat{v}_{uv} can be regarded as the estimated version of v_{uv}^* . Considering the relationship of $\hat{\mathbf{W}}_{uv}^{(ijk)}$ and $\hat{\mathbf{W}}_{uv}^{\#(ijk)}$, the corresponding variance of $\hat{\mathbf{W}}_{uv}^{(ijk)}$ is Eq. (14) providing a closed-form variance describing the confidence of $\hat{\mathbf{W}}_{uv}^{(ijk)}$. Therefore, the variance of $\hat{\mathbf{W}}_{uv}^{(ijk)}$ is:

$$\sigma_{\xi}^{(ijk)2} = \text{Var}(\hat{\mathbf{W}}_{uv}^{(ijk)} - \mathbf{W}_{uv}^{\#(ijk)}) \approx g^{-1}(\sigma_0^2 \hat{v}_{uv}) \quad (14)$$

where $g^{-1}(\cdot)$ is the inverse permutation function of $g(\cdot)$. $\xi \subseteq \{1, \dots, M\} \times \{1, \dots, N\} \times \{1, \dots, P\}$ is the corresponding 3D index of uv at patch (ijk) .

III. RESULTS AND DISCUSSION

We validate the proposed method on the Indian Pines dataset (simulation dataset) ¹. This Indian Pines dataset is the subset of the data gathered by the AVIRIS sensor. It consists of 145×145 pixels and 224 spectral reflectance bands in the

¹<https://engineering.purdue.edu/biehl/MultiSpec/hyperspectral.html>



(a)

Fig. 3: This is the false-color image of the Indian dataset with bands composed of the bands 10, 37 and 70. This is the manually classified ground truth of the Indian dataset.

TABLE I: The coverage rates of $\text{Var}(\hat{\mathbf{W}}_{uv}^{(l)} - \overline{\mathbf{W}}_{uv}^{\#})$ for different σ_0 over 100 Monte Carlo trials. “std” denotes the standard deviation. The proposed closed-form uncertainty estimation approach describes the probability distribution well.

σ_0	Indian	
	Mean	Std
0.075	0.9579	0.0371
0.050	0.9576	0.0383
0.100	0.9643	0.0319
0.125	0.9704	0.0273

wavelength range of $0.42.510^{-6}$ meters and covers the Indian Pines test site in North-western Indiana. The Indian Pines scene contains two-thirds agriculture, and one-third forest or other natural perennial vegetation. We adopt the ground truth of the Indian Pines dataset and simulate with arbitrary Gaussian noise.

To provide convincing validations, we strictly follow the parameter and noise setting of the selected baseline method [18]. The size of the sliding window is $20 \times 20 \times P$ where P are the number of bands of the dataset. The step size is 4 and the rank r is set to 7. In the image restoration process, all images are normalized to range $[0, 1]$. In the noise simulation process, the zero-mean Gaussian noise is uniformly imposed on all pixels of the datasets with different levels of noise. We further test the impact of impulse noise on the dataset.

A. The validation of the accurate uncertainty description

The accuracy of the proposed closed-form uncertainty quantification method is extensively validated with numerical Monte Carlo tests. We impose different levels of Gaussian noises on the HSI. A large number of numerical experiments provide enough samples to test if the statistical distributions of those samples are described accurately with the proposed closed-form variance. Specifically, $T = 100$ times of Monte Carlo tests are performed on the chosen variance σ_0^2 . For each element of the estimated HSI in trial l at position $[u, v, c]$ as $\hat{\mathbf{W}}_{uv}^{(l)}$, we define its deviation to the corresponding T times mean value as $\overline{\mathbf{W}}_{uv}^{\#}$. The deviation to the mean is defined as:

$$e_{uv}^{(l)} = \|\hat{\mathbf{W}}_{uv}^{(l)} - \overline{\mathbf{W}}_{uv}^{\#}\|, \quad l \in [1, \dots, 100] \quad (15)$$

TABLE II: The probability values (p -value) of the Shapiro-Wilk test of datasets Indian. We cite the corresponding element position of Fig. (4) as an example through all the tests. The p -value > 0.05 indicates a significant possibility that the element is normally distributed.

Dataset	Indian
0.050	0.4239
0.075	0.1103
0.100	0.8498
0.125	0.4346

If the estimation also follows the statistical distribution and the closed-form solution describes statistical distribution of the estimation well, 95% of $\hat{\mathbf{W}}_{uv}^{(l)}$ should fall within the range of $[\overline{\mathbf{W}}_{uv}^{\#} - 1.96\hat{\sigma}_{uv}, \overline{\mathbf{W}}_{uv}^{\#} + 1.96\hat{\sigma}_{uv}]$. Following Eq. (15), we define the ratio of $e_{uv}^{(l)}$ falls within the $1.96\hat{\sigma}_{uv}$ bound as the element-wise coverage rate **coverage rate**. The average of all elements' **coverage rate** is the **average coverage rate**.

We present the average general statistical results over all elements of the 3 datasets in table I, and it indicates that the closed-form uncertainty quantification coverage rate is close to 95%. All the results indicate that the **average coverage rate** is not far away from 95% and the variance of the ratio is low.

B. The validation of the normal distribution of the restored HSI

On top of the **average coverage rate** of the variance, we also adopt the Monte-Carlo experiments to prove that the restored HSI $\hat{\mathbf{W}}^{(l)}$ has innate Gaussian distribution. Both quantile-quantile (Q-Q) plots and Shapiro-Wilk tests are conducted to validate our claim. Fig. 4 demonstrates the (Q-Q) plots of all the datasets. Note that we randomly plot one element of each dataset as an example, but all other elements are similar since the observation is isotropic. Fig. 4 indicates that the Monte-Carlo estimation of all the trials $\hat{\mathbf{W}}^{(l)}$ is close to a line, thus follows the Gaussian distribution.

We also conduct another routine test, the Shapiro-Wilk tests, to validate the claim that the estimations follow the Gaussian distribution. Since it is not possible to present all the elements, we randomly choose element position over the three datasets with different levels of Gaussian noise. The results are presented in Table II. The p -value indicates that all samples are significantly following the normal distribution (> 0.05). Since all elements of the shape should be consistent (either obey or reject the normal distribution), we can conclude that the shape obeys the normal distribution.

IV. CONCLUSION

This is the first research to discuss the uncertainty quantification for LRMA based HSI denoising techniques. We provide a time-efficient closed-form uncertainty propagation model to quantify the element-wise uncertainty for the denoised HSI without any prior ground-truth. Moreover, the proposed uncertainty estimation approach is independent of the choice of the LRMA algorithm. It is based on the global minimum assumption of LRMA, thus more accurate algorithm

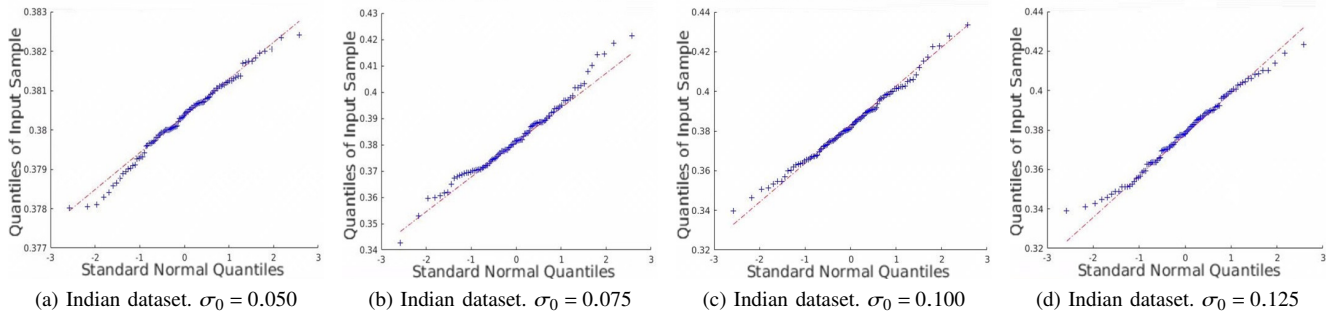


Fig. 4: Illustrated are the Q-Q plots of a random element position over 100 independent trials for noise in the dataset.

leads to better performance of the uncertainty estimation. Extensive numerical experiments indicate that the proposed uncertainty quantification method is accurate and robust to describe the statistical behaviors of the estimations from the LRMA approach. The time consumption of the closed-form formulation is almost negligible to be deployed to any state-of-the-art LRMA algorithms. The uncertainty provided by our approach can be further applied to applications that require multi-source or multi-scale data fusion, data assimilation and product confidence estimation.

REFERENCES

- [1] H. Dehghan and H. Ghassemian, "Measurement of uncertainty by the entropy: application to the classification of mss data," *International journal of remote sensing*, vol. 27, no. 18, pp. 4005–4014, 2006.
- [2] G. M. Foody and P. M. Atkinson, *Uncertainty in remote sensing and GIS*. John Wiley & Sons, 2003.
- [3] X. Chen, K. Yu, and H. Wu, "Determination of minimum detectable deformation of terrestrial laser scanning based on error entropy model," *IEEE Transactions on Geoscience and Remote Sensing*, vol. 56, no. 1, pp. 105–116, 2017.
- [4] X. Du and A. Zare, "Multiresolution multimodal sensor fusion for remote sensing data with label uncertainty," *IEEE Transactions on Geoscience and Remote Sensing*, 2019.
- [5] A. Oxley, *Uncertainties in GPS Positioning: A mathematical discourse*. Academic Press, 2017.
- [6] L. Bastin, P. F. Fisher, and J. Wood, "Visualizing uncertainty in multi-spectral remotely sensed imagery," *Computers & Geosciences*, vol. 28, no. 3, pp. 337–350, 2002.
- [7] E. Sarhrouni, A. Hammouch, and D. Aboutajdine, "Application of symmetric uncertainty and mutual information to dimensionality reduction and classification of hyperspectral images," *arXiv preprint arXiv:1211.0613*, 2012.
- [8] Y. Zhou, A. Rangarajan, and P. D. Gader, "A spatial compositional model for linear unmixing and endmember uncertainty estimation," *IEEE Transactions on Image Processing*, vol. 25, no. 12, pp. 5987–6002, 2016.
- [9] M.-E. Polo, Á. M. Felicísimo, A. G. Villanueva, and J.-Á. Martínez-del Pozo, "Estimating the uncertainty of terrestrial laser scanner measurements," *IEEE transactions on geoscience and remote sensing*, vol. 50, no. 11, pp. 4804–4808, 2012.
- [10] P. Ghamisi, N. Yokoya, J. Li, W. Liao, S. Liu, J. Plaza, B. Rasti, and A. Plaza, "Advances in hyperspectral image and signal processing: A comprehensive overview of the state of the art," *IEEE Geoscience and Remote Sensing Magazine*, vol. 5, no. 4, pp. 37–78, 2017.
- [11] Q. Zhang, Q. Yuan, J. Li, X. Liu, H. Shen, and L. Zhang, "Hybrid noise removal in hyperspectral imagery with a spatial-spectral gradient network," *IEEE Transactions on Geoscience and Remote Sensing*, vol. 57, no. 10, pp. 7317–7329, 2019.
- [12] A. Buades, B. Coll, and J.-M. Morel, "A non-local algorithm for image denoising," in *2005 IEEE Computer Society Conference on Computer Vision and Pattern Recognition (CVPR'05)*, vol. 2. IEEE, 2005, pp. 60–65.
- [13] M. Maggioni, V. Katkovnik, K. Egiazarian, and A. Foi, "Nonlocal transform-domain filter for volumetric data denoising and reconstruction," *IEEE transactions on image processing*, vol. 22, no. 1, pp. 119–133, 2012.
- [14] Y. Qian and M. Ye, "Hyperspectral imagery restoration using nonlocal spectral-spatial structured sparse representation with noise estimation," *IEEE Journal of Selected Topics in Applied Earth Observations and Remote Sensing*, vol. 6, no. 2, pp. 499–515, 2012.
- [15] K. Dabov, A. Foi, V. Katkovnik, and K. Egiazarian, "Image denoising by sparse 3-d transform-domain collaborative filtering," *IEEE Transactions on image processing*, vol. 16, no. 8, pp. 2080–2095, 2007.
- [16] Q. Yuan, L. Zhang, and H. Shen, "Hyperspectral image denoising employing a spectral-spatial adaptive total variation model," *IEEE Transactions on Geoscience and Remote Sensing*, vol. 50, no. 10, pp. 3660–3677, 2012.
- [17] J. Li, Q. Yuan, H. Shen, and L. Zhang, "Noise removal from hyperspectral image with joint spectral-spatial distributed sparse representation," *IEEE Transactions on Geoscience and Remote Sensing*, vol. 54, no. 9, pp. 5425–5439, 2016.
- [18] H. Zhang, W. He, L. Zhang, H. Shen, and Q. Yuan, "Hyperspectral image restoration using low-rank matrix recovery," *IEEE Transactions on Geoscience and Remote Sensing*, vol. 52, no. 8, pp. 4729–4743, 2013.
- [19] L. Zhuang and J. M. Bioucas-Dias, "Fast hyperspectral image denoising and inpainting based on low-rank and sparse representations," *IEEE Journal of Selected Topics in Applied Earth Observations and Remote Sensing*, vol. 11, no. 3, pp. 730–742, 2018.
- [20] W. He, H. Zhang, L. Zhang, and H. Shen, "Hyperspectral image denoising via noise-adjusted iterative low-rank matrix approximation," *IEEE Journal of Selected Topics in Applied Earth Observations and Remote Sensing*, vol. 8, no. 6, pp. 3050–3061, 2015.
- [21] Q. Yuan, Q. Zhang, J. Li, H. Shen, and L. Zhang, "Hyperspectral image denoising employing a spatial-spectral deep residual convolutional neural network," *IEEE Transactions on Geoscience and Remote Sensing*, vol. 57, no. 2, pp. 1205–1218, 2018.
- [22] W. He, H. Zhang, L. Zhang, and H. Shen, "Total-variation-regularized low-rank matrix factorization for hyperspectral image restoration," *IEEE transactions on geoscience and remote sensing*, vol. 54, no. 1, pp. 178–188, 2015.
- [23] J. M. Bioucas-Dias and J. M. Nascimento, "Hyperspectral subspace identification," *IEEE Transactions on Geoscience and Remote Sensing*, vol. 46, no. 8, pp. 2435–2445, 2008.
- [24] Y. Chen, X. Cao, Q. Zhao, D. Meng, and Z. Xu, "Denoising hyperspectral image with non-iid noise structure," *IEEE transactions on cybernetics*, vol. 48, no. 3, pp. 1054–1066, 2017.
- [25] H. Fan, C. Li, Y. Guo, G. Kuang, and J. Ma, "Spatial-spectral total variation regularized low-rank tensor decomposition for hyperspectral image denoising," *IEEE Transactions on Geoscience and Remote Sensing*, vol. 56, no. 10, pp. 6196–6213, 2018.
- [26] Y. Chen, W. He, N. Yokoya, and T.-Z. Huang, "Hyperspectral image restoration using weighted group sparsity-regularized low-rank tensor decomposition," *IEEE transactions on cybernetics*, 2019.
- [27] B. Aiazzi, L. Alparone, A. Barducci, S. Baronti, P. Marcoionni, I. Pippi, and M. Selva, "Noise modelling and estimation of hyperspectral data from airborne imaging spectrometers," *Annals of Geophysics*, vol. 49, no. 1, 2006.
- [28] N. Acito, M. Diani, and G. Corsini, "Signal-dependent noise modeling and model parameter estimation in hyperspectral images," *IEEE Trans-*

- actions on Geoscience and Remote Sensing*, vol. 49, no. 8, pp. 2957–2971, 2011.
- [29] Y. Chen, J. Fan, C. Ma, and Y. Yan, “Inference and uncertainty quantification for noisy matrix completion,” *arXiv preprint arXiv:1906.04159*, 2019.
- [30] J. Wright, A. Ganesh, S. Rao, Y. Peng, and Y. Ma, “Robust principal component analysis: Exact recovery of corrupted low-rank matrices via convex optimization,” in *Advances in neural information processing systems*, 2009, pp. 2080–2088.
- [31] T. Zhou and D. Tao, “Godec: Randomized low-rank & sparse matrix decomposition in noisy case,” in *Proceedings of the 28th International Conference on Machine Learning, ICML 2011*, 2011.